nature photonics

Article

https://doi.org/10.1038/s41566-024-01539-3

Unified laser stabilization and isolation on a silicon chip

Received: 20 February 2024

Accepted: 28 August 2024

Published online: 15 October 2024

Check for updates

Alexander D. White[1,4] ✉, Geun Ho Ahn[1,4] ✉, Richard Luhtaru[1], Joel Guo[2], Theodore J. Morin[2], Abhi Saxena[3], Lin Chang[2], Arka Majumdar[3], Kasper Van Gasse[1], John E. Bowers[2] & Jelena Vučković[1]

Rapid progress in photonics has led to an explosion of integrated devices that promise to deliver the same performance as table-top technology at the nanoscale, heralding the next generation of optical communications, sensing and metrology, and quantum technologies. However, the challenge of co-integrating the multiple components of high-performance laser systems has left application of these nanoscale devices thwarted by bulky laser sources that are orders of magnitude larger than the devices themselves. Here we show that the two main components for high-performance lasers—noise reduction and isolation—can be sourced simultaneously from a single, passive, CMOS-compatible nanophotonic device, eliminating the need to combine incompatible technologies. To realize this, we take advantage of both the long photon lifetime and the non-reciprocal Kerr nonlinearity of a high-quality-factor silicon nitride ring resonator to self-injection lock a semiconductor laser chip while also providing isolation. We also identify a previously unappreciated power regime limitation of current on-chip laser architectures, which our system overcomes. Using our device, which we term a unified laser stabilizer, we demonstrate an on-chip integrated laser system with built-in isolation and noise reduction that operates with turnkey reliability. This approach departs from efforts to directly miniaturize and integrate traditional laser system components and serves to bridge the gap to fully integrated optical technologies.

Coherent optical sources serve as the backbone of optical communication, sensing and metrology, and quantum technologies[1–3]. Long coherence times and narrow linewidths allow for more precise heterodyne detection, interferometry and probing of atomic transitions. Traditionally, the narrow linewidth optical sources required for these applications are built from table-top laser systems, but technological innovation in optical networking[4,5], data processing[6–8], light detection and ranging[9–11], and chip-scale quantum computers[12–14] demand the same performance from compact and fully integrated systems. In this vein, considerable efforts have been made to miniaturize and integrate the components of low-noise lasers. Three key components must be combined to achieve this: a semiconductor gain chip or laser; an external cavity for linewidth stabilization; and an optical isolator to prevent unwanted reflections from destabilizing the laser.

Integrated III–V semiconductor lasers form the backbone of the internet, and their power, linewidth and stability have been continuously improving over the past few decades. However, to further improve linewidth and to increase tunability and stability, it is necessary to couple lasers with additional photonic components. Although III–V materials such as InP and GaAs serve as excellent gain media,

[1]E. L. Ginzton Laboratory, Stanford University, Stanford, CA, USA. [2]ECE Department, University of California, Santa Barbara, CA, USA. [3]ECE Department, University of Washington, Seattle, WA, USA. [4]These authors contributed equally: Alexander D. White, Geun Ho Ahn. ✉e-mail: adwhite@stanford.edu; gahn@stanford.edu

https://doi.org/10.1038/s41566-024-01539-3

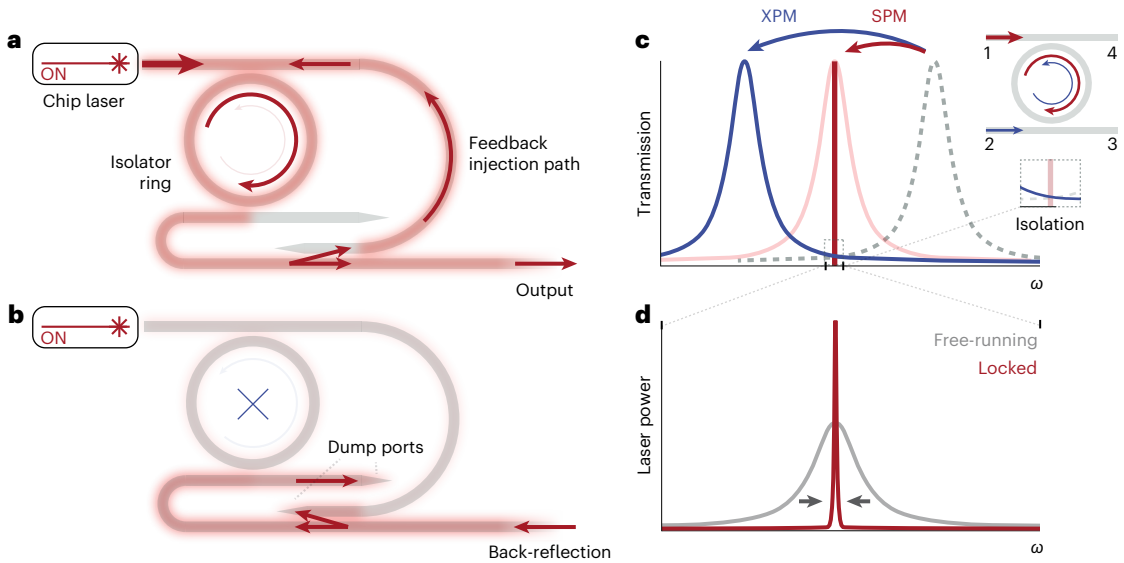

Fig. 1 | Theory of operation. a, Device schematic. A chip laser pumps an isolator ring, whose output is tapped off to provide feedback to the laser. As the ring is being pumped in the clockwise direction, the power travelling from the feedback injection path to the laser is not resonant with the anticlockwise mode of the ring and travels back fully into the laser, stabilizing it. **b**, The device under the influence of back-reflection. Back-reflected power (in a frequency band near the pump) is not resonant with the anticlockwise mode of the ring and gets dumped, unable to reach the laser. **c**, Transmission spectrum of the isolator ring in the clockwise (red) and anticlockwise (blue) modes. The grey dashed curve shows the degenerate cold cavity spectrum of the ring. This splitting is due to the twofold difference in strength between SPM and XPM in the ring. **d**, Effect of the feedback on the laser linewidth.

their processing complexity leads to large waveguide losses and incompatibility with complementary metal–oxide–semiconductor (CMOS) processing, rendering monolithic integration of photonic devices in III–V undesirable[15]. Furthermore, although some types of semiconductor lasers are less sensitive to back-reflection[16–18], they are still in the regime in which optical isolators are critical for preventing destabilization[19].

Extremely-high-quality-factor ($Q > 2 \times 10^8$) silicon nitride ring cavities have recently been used in conjunction with chip-scale semiconductor lasers to achieve hertz-level linewidths on an integrated platform[20,21], rivalling even the best-performing table-top systems. These devices work by taking advantage of the naturally occurring back-scattering in high-Q resonators to provide narrow linewidth feedback that self-injection locks a semiconductor laser. As back-scattering is nearly ubiquitous in high-Q resonators, this approach is reliable even though it is not deterministic. However, as we will show in this paper, this technique starts to break down when power levels in the device are high enough to access nonlinear processes in the resonator material. This effect imposes stringent limits on the maximum operating power and quality factor of current architectures. Furthermore, these devices still require external isolators.

Integrated isolators have also made considerable strides recently, with demonstrations of on-chip isolators approaching the performance of stand-alone optical elements[22,23]. However, there are substantial challenges in integrating these with low-noise systems. For instance, resonant devices[22,24] would require the tuning of multiple high-Q resonators to degenerate frequencies. Meanwhile, non-resonant devices can be quite large (>1 cm) and, without a resonant filter, only provide a frequency shift of the back-reflected power reaching the laser cavity[23]. Although this has been shown to prevent laser destabilization, it is not clear whether it would allow for the preservation of an ultra-narrow linewidth.

Despite this great progress in the integration of individual laser components, there is not a clear path to co-integrate them because they are built using disparate and often incompatible technological platforms. As a result, fully integrated laser systems remain elusive. This necessitates driving photonic integrated circuits with external sources that are often orders of magnitude larger than the circuits themselves[4–14].

Here we propose and demonstrate a single CMOS-compatible device—which we term a unified laser stabilizer (ULS)—that passively and simultaneously feedback-stabilizes and isolates semiconductor lasers. To realize this device, we use the high quality factor of a ring resonator as a resource for both long photon lifetimes and optical nonlinearity. Long photon lifetimes allow us to generate linewidth reduction through self-injection locking, and optical nonlinearity allows us to generate optical isolation through the non-reciprocal Kerr effect. Operating the ring resonator as a circulator, we can deterministically provide strong feedback (and thus large linewidth reductions) independent of input power, enabling concurrent linewidth narrowing and isolation. As the isolation and feedback come from the same ring, the laser is always on resonance, relaxing system complexity and enabling turnkey operation.

Theory of operation

High-quality-factor ring resonators can be used to directly isolate the output of a continuous-wave laser[25–27]. This works by taking advantage of the non-reciprocity of the optical Kerr effect (third-order nonlinearity $\chi^{(3)}$). When one of the degenerate clockwise and anticlockwise modes of a ring is pumped, the differential action of self-phase modulation (SPM) and cross-phase modulation (XPM) induce a differential shift in the clockwise and anticlockwise resonance frequencies, respectively. As XPM is twice as strong as SPM, the ring mode counter-propagating with respect to the pump is shifted twice as far in frequency as the pump mode, leading to the split transmission spectrum illustrated in Fig. 1c. The pump can then transmit through the ring with near-unity efficiency, while any power reflected back is no longer resonant with the ring, and is thus isolated.

The maximum isolation achieved with this scheme can be found by taking the Lorentzian transmission of the detuned resonance[26,27]:

$$I = \frac{1}{1 + (2Q\frac{\Delta\omega}{\omega_0})^2}, \quad (1)$$

https://doi.org/10.1038/s41566-024-01539-3

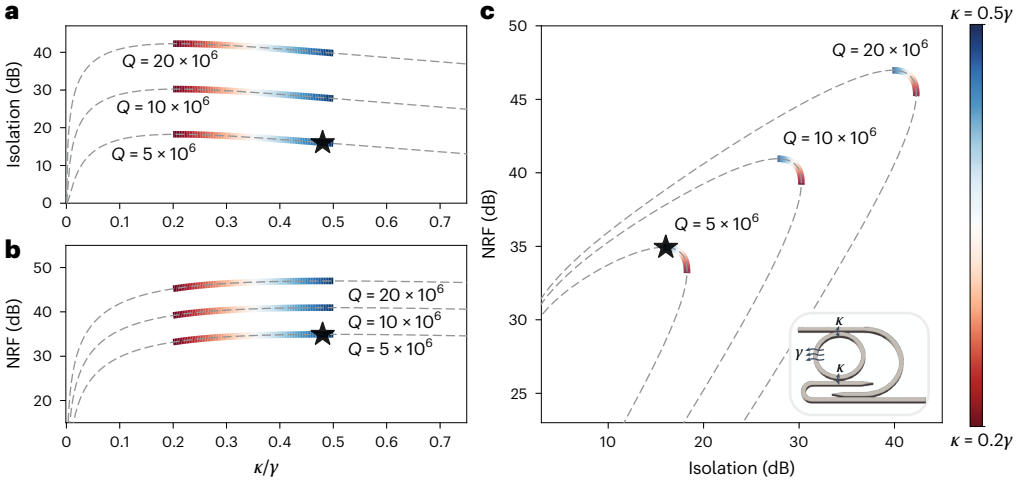

Fig. 2 | Isolation versus NRF tradeoff. a, Theoretical isolation as a function of the ratio of κ to γ for a range of state-of-the-art intrinsic Q factors, where $n_2/n = 1.2 \times 10^{-19}$ m^2 W^{-1} and $V_{mode} = 1{,}800$ μm^3. **b**, Theoretical NRF as a function of the ratio of ring coupling rate κ to loss rate γ, where $Q_{laser} = 5 \times 10^4$, laser amplitude phase coupling $\alpha = 2.5$, and return loss $\Gamma = 20$ dB when $\kappa = 0.5\gamma$. **c**, Isolation versus NRF tradeoff for a range of intrinsic Q factors. Stars indicate the κ values demonstrated in this work. Inset shows device schematic illustrating coupling and loss rates.

$$\Delta\omega = \omega_0 \frac{n_2}{n} \frac{Q\lambda}{2\pi V_{mode}} \eta P_{in}, \tag{2}$$

where ω_0 is the original resonance frequency of the ring, n_2 is the nonlinear refractive index, n is the linear refractive index, Q is the loaded quality factor of the ring, V_{mode} is the mode volume of the ring, η is the coupling efficiency of the pump to the ring, and P_{in} is the input power. At the peak of the forward resonance, where isolation is maximized, the coupling efficiency $\eta = \frac{4\kappa_1(\kappa_2+\gamma)}{(\kappa_1+\kappa_2+\gamma)^2}$ depends on the coupling rates κ_1 and κ_2, and the intrinsic loss rate γ. As the isolation ratio scales as Q^4, it is highly desirable to operate with a large quality factor (>10^6). This not only ensures the maximum possible isolation, but also reduces the power threshold required to induce isolation.

Although it serves to provide isolation, the high-quality-factor ring can also be used as a resource for frequency stability. This is achieved by coupling the semiconductor laser to the high-Q resonator through feedback, effectively creating an external cavity laser (ECL)[20,21]. As the fundamental coherence limit of a laser, given by the Schawlow–Townes linewidth[28]

$$\Delta\nu_{laser} \geq \frac{\pi h\nu(\Delta\nu_{cav})^2}{P_{out}} = \frac{\pi h\nu^3}{Q^2 P_{out}}, \tag{3}$$

(where h is Planck's constant, ν is the laser frequency and P_{out} is the laser power), is dependent on Q, the fundamental frequency noise of a laser can be reduced by the introduction of high-Q feedback by the noise reduction factor (NRF)

$$\mathrm{NRF} \propto \Gamma \frac{(Q_{cav})^2}{(Q_{laser})^2}, \tag{4}$$

where Γ is the fraction of power fed back to the laser. As semiconductor chip lasers typically have a low quality factor ($Q_{laser} \approx 10^4$) to maximize their output power, we can use the high-quality-factor rings ($Q_{cav} > 10^6$) to reduce their frequency noise by orders of magnitude. For the remainder of the paper, we use Q to denote the loaded cavity quality factor (labelled Q_{cav} above).

We propose the topology illustrated in Fig. 1a to achieve simultaneous isolation and feedback stabilization, and we refer to this set-up as a unified laser stabilizer. A chip laser is coupled to an isolator ring, which transmits power in the clockwise mode to an output waveguide. This output waveguide is tapped off with a directional coupler and a fraction of the power is fed back to the laser. To reach the laser, the feedback power has to pass by the ring. As it is now travelling in the opposite direction, it interacts only with the detuned anticlockwise mode, preventing power coupling to the ring and allowing full transmission back to the laser. Meanwhile, any back-reflected power is off-resonant with the ring and gets dumped, preventing it from reaching the laser diode (Fig. 1b). Here the ring effectively acts as a circulator. If the ring is critically coupled ($\kappa_1 = \kappa_2 \gg \gamma$), transmission is only allowed from ports 1 → 2 → 3 → 4 → 1 (as labelled in Fig. 1c). If the ring is not critically coupled, the allowed transmission is 1 → 2 ↔ 3 → 4 ↔ 1. The circulator behaviour allows a large fraction of the output power to be fed back to the laser diode, leading to a strong reduction in the laser linewidth (Fig. 1d).

There are several important design considerations for optimizing the isolation and noise reduction of a ULS, most notably ring loading, resonator mode volume and feedback strength. Of course, as the isolation and NRF scale as a function of Q^4 and Q^2, respectively, improving Q will greatly improve the all-around performance. Given a fixed intrinsic Q, there are direct tradeoffs.

First, due to their different scaling, the isolation and NRF have different optimal loadings of the ring. To maximize isolation, one should maximize $Q^2\eta = (\frac{1}{\kappa_1+\kappa_2+\gamma})^2 \frac{4\kappa_1(\kappa_2+\gamma)}{(\kappa_1+\kappa_2+\gamma)^2}$, where κ_1 and κ_2 are the coupling rates of the ring to the two waveguides, and γ is the intrinsic loss rate of the ring. For $\kappa_1 = \kappa_2$, this leads to an optimum of $\kappa = \frac{\sqrt{2}-1}{2}\gamma$ (Fig. 2a). To maximize NRF, one should maximize $Q^2\Gamma = (\frac{1}{\kappa_1+\kappa_2+\gamma})^2 \frac{4\kappa_1\kappa_2}{(\kappa_1+\kappa_2+\gamma)^2}$, which, with $\kappa_1 = \kappa_2$, leads to an optimum of $\kappa = 0.5\gamma$ (Fig. 2b)—approximately 2.5 times more loaded than the isolation optimum. Outside of this range ($0.2\gamma < \kappa < 0.5\gamma$), the isolation and NRF reduce together (Fig. 2c).

Furthermore, although the mode volume does not directly affect the NRF, it does affect the thermorefractive noise (TRN) limit of the linewidth reduction (Supplementary Section 1). The thermal limit of noise reduction scales linearly with mode volume[29], whereas isolation scales inversely, creating a tradeoff between isolation and the TRN limit. As input power increases isolation without greatly affecting the NRF or TRN limit, the mode volume can therefore be traded off with input power. Finally, as the feedback strength is deterministic, it can be tuned with the coupling ratio of the directional coupler to trade between maximum output power and the NRF. Again, the noise

https://doi.org/10.1038/s41566-024-01539-3

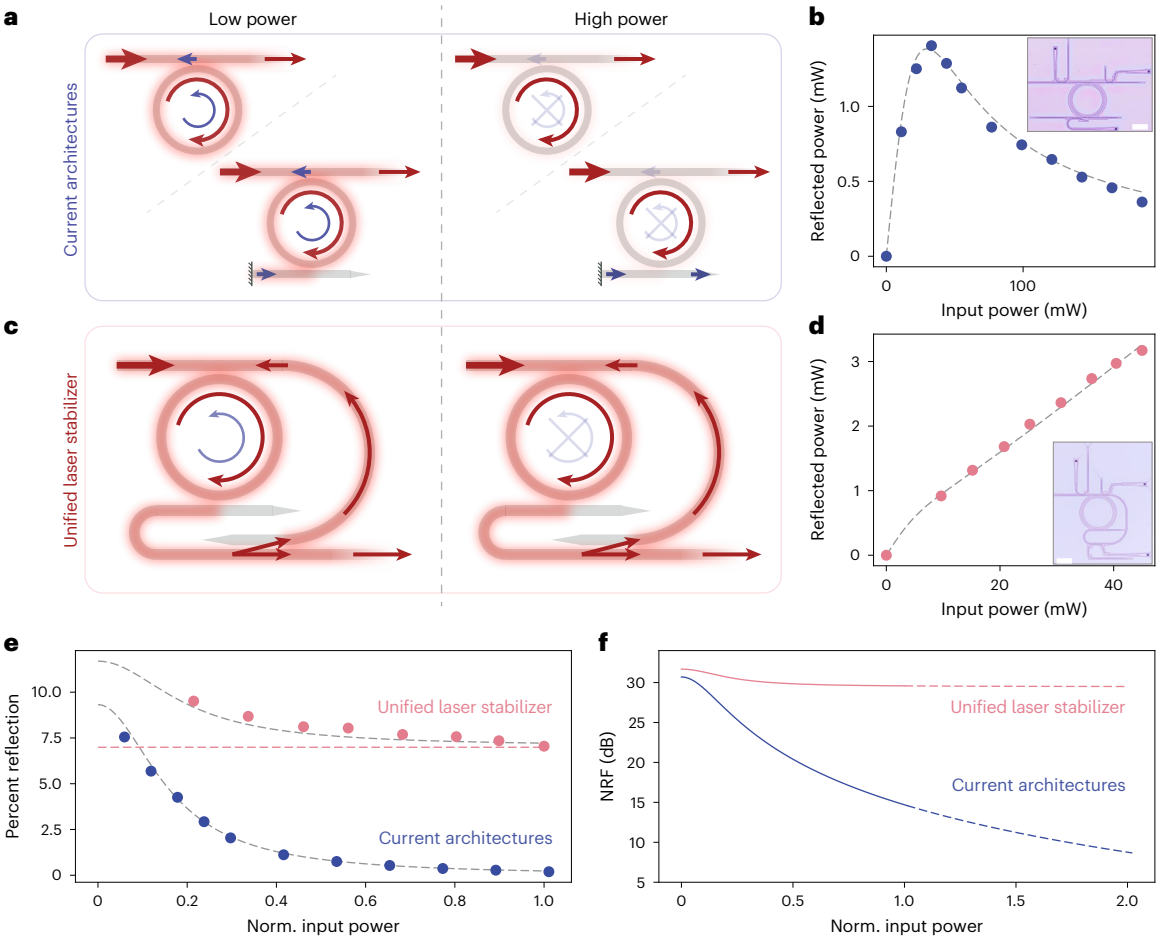

Fig. 3 | High-*Q* feedback. a, Current self-injection-locking architectures, based on parasitic or intentional back-scattering. Intrinsic ring back-scattering or a reflector are used to generate feedback signal. At low power, this works well, but as the power increases, the backscattered power no longer reaches the laser. **b**, Theoretical (dashed line) and experimental (data points) back-reflection as a function of input power corresponding to the architectures in **a**. At low powers, the device is linear and exhibits a constant back-reflection ratio, but as power increases, the nonlinear resonance splitting substantially attenuates the back-reflection. The inset is an image of the device (scale bar, 100 µm). **c**, The ULS feedback architecture. Substantial feedback is provided back to the laser regardless of input power. **d**, Theoretical (dashed line) and experimental (data points) back-reflection as a function of input power corresponding to the architecture in **c**. The back-reflection strength is nearly independent of input power, with slight deviation arising from intrinsic back-scattering in the ring which is attenuated at higher powers. The inset is an image of the device (scale bar, 100 µm). **e**, Back-reflection as a percentage of input power for ULS and current architectures. The pink dashed line illustrates the asymptotic limit of the ULS reflection for high input powers. Due to different device quality factors, input power is normalized so that maximum input power corresponds to 15 dB isolation (45 mW for ULS and 185 mW for current architecture due to a lower *Q* factor). **f**, Theoretical NRF versus input power for each architecture assuming equivalent quality factors and insertion losses. The dashed lines are projections for higher power levels.

reduction is ultimately limited by the TRN, and thus it cannot be maximized arbitrarily.

As every system has different noise, power and isolation requirements, the optimal device configuration will probably be very different in each scenario. In this paper we chose to load the devices to $\kappa = 0.5\gamma$ (indicated by stars in Fig. 2) and feed back 50% of the out-coupled power to demonstrate a relatively low-power device with good isolation and a high NRF.

High-*Q* stability

In addition to providing simultaneous isolation and noise reduction, the ULS topology solves a critical issue for self-injection-locked lasers. Current schemes rely on either parasitic back-reflection in rings[20,21,30–33], or a reflector placed after port 2 of the ring (drop port)[34,35] (Fig. 3a). Although these have been quite effective in low-power or low-*Q* regimes, these schemes rely on the coupling and degeneracy of the clockwise and anticlockwise modes of the ring. If the power or *Q* increased enough to break this degeneracy and provide isolation, the feedback strength would be heavily attenuated. As NRF is proportional to feedback strength, this attenuated power would lead to a dramatic reduction in efficacy of these systems (Supplementary Sections 2 and 3). Using published device parameters, we calculate at which power level and *Q* factor these state-of-the-art injection-locked lasers[20,30–32,34–40] will begin to fail (Supplementary Section 4). In many cases, these failure points are within an order of magnitude of the current operating point.

In Fig. 3b we show the theoretical and experimental power-dependent back-reflection of a ring. Intrinsic back-scattering in the ring couples the clockwise and anticlockwise modes, causing a fraction of the input power to reflect. At low input power, the back-reflected power increases linearly with the input power. As the input power increases, however, the clockwise and anticlockwise modes become increasingly detuned, and therefore less power is coupled backwards. This reduction is equal to the isolation ratio of the ring, here reaching a maximum of 15 dB.

By instead providing non-reciprocal feedback through the ring (Fig. 3c), we can achieve a nearly linear response even at high input powers. In Fig. 3d we show the back-reflected power for a device with

https://doi.org/10.1038/s41566-024-01539-3

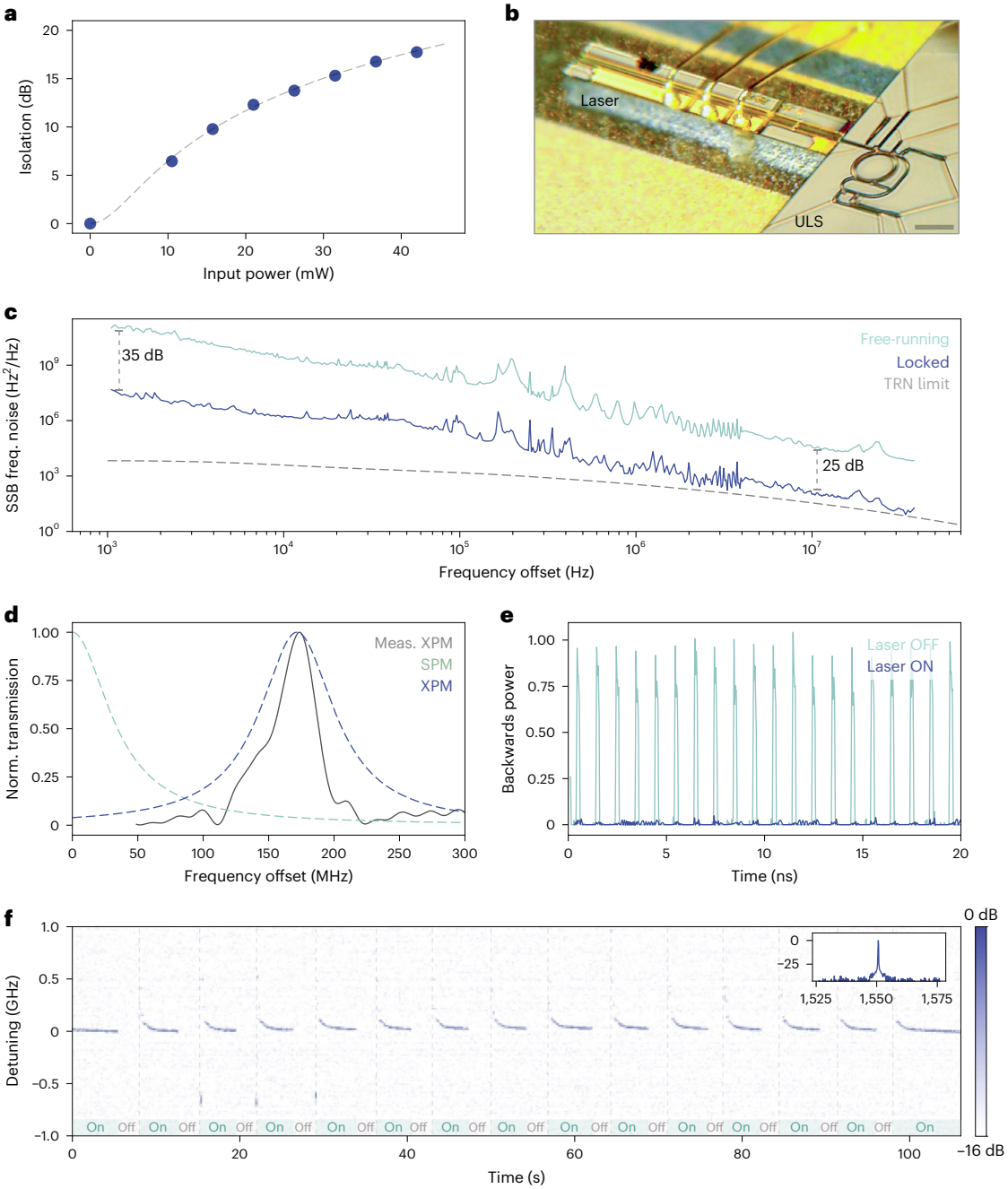

Fig. 4 | Device performance. a, Isolation versus input power measured with a tunable ECL. **b**, Device image showing hybrid integration of a DFB laser and ULS. Scale bar, 200 µm. **c**, Single sideband frequency (SSB freq.) noise power spectral density of the laser when free running or when locked to the ULS device. The grey dashed line represents the simulated thermorefractive noise of the device. **d**, Measurement of the nonlinear splitting when locked to a semiconductor DFB laser with 33 mW of input power. The grey trace shows the normalized backward transmission of the device (measured XPM resonance; see Methods for measurement details). The dashed lines show the theoretical transmission spectrum of the SPM and XPM resonances calculated from this measurement and from measurements of the ring linewidth. This splitting corresponds to an isolation ratio of 14 dB. **e**, Measurement of backward transmission of 10 MHz pulses with the chip laser off (with the signal at the peak of the resonance) or on and locked to the ring (with the signal at the same frequency as the chip laser). **f**, Spectrograph of the heterodyne beat note between an isolated chip laser (operating in a continuous-wave regime) and a tunable ECL across numerous power cyclings. The laser current driver was turned on and off fully each cycle. Vertical lines correspond to the driver being switched on. The inset shows the corresponding optical spectrum.

this new topology, which also exhibits 15 dB of isolation. Here less input power is needed due to a higher Q factor. At low input power, there are three competing effects: the intrinsic ring back-scattering, the feedback through the ring, and the filtering the ring does to this feedback. At high power, however, the intrinsic back-scattering and feedback filtering are attenuated by the isolation ratio, allowing for a linear response (Supplementary Section 5). We compare the measured back-scattering ratio and the corresponding theoretical NRFs of these topologies in Fig. 3e,f. With current back-scattering-based schemes, the presence of isolation directly degrades the NRF and locking range[41] (proportional to the isolation ratio and square root of the isolation ratio, respectively), destroying its stabilization capability. In contrast, the unified laser stabilization topology preserves the high NRF across all power levels.

Device integration and measurement

We implement the ULS using a silicon nitride on insulator platform. Although these devices are currently fabricated in-house, ultra-high-Q silicon nitride photonics is fully compatible with foundry CMOS processes, as demonstrated in refs. 33,42, making scalable integration of these devices practical. We use a 310 nm waveguide height-controlled by low-pressure chemical vapour deposition of silicon nitride to maintain a normal dispersion profile and prevent parasitic nonlinear conversion processes. We use multi-mode rings (4 μm wide) and clad the devices with a thick oxide layer through plasma-enhanced chemical vapour deposition to enable high quality factors (Supplementary Section 6).

We first measure the isolation of the ULS with a tunable ECL (Fig. 4a). At each input power, we tune the laser across the ring resonance and record the backward transmission at the resonance peak. As expected, the isolation ratio follows a Lorentzian power-dependent curve proportional to the nonlinear detuning. We then edge-couple the ULS device to a semiconductor distributed-feedback (DFB) laser that provides a coupled on-chip power of approximately 33 mW (Fig. 4b). With a correlated self-heterodyne set-up as described in ref. 43, we measure the single sideband frequency noise power spectral density (Fig. 4c). Compared with the free-running DFB laser, our hybrid device displays a noise reduction of 25–35 dB, limited at high offset frequency by the TRN of the ring. At high frequency offset, close to the white noise floor of the laser, the single sideband frequency noise power spectral density is reduced from 8,200 Hz^2/Hz to 14 Hz^2/Hz, corresponding to instantaneous linewidths of 51 kHz and 89 Hz, respectively (Supplementary Sections 7 and 9).

We then verify that isolation is achieved simultaneously with this reduction in frequency noise using two independent methods. First, we directly measure the nonlinear splitting of the ring modes, taking a similar approach to ref. 27, modified to include a DFB pump. To generate a probe signal, we take a tunable ECL and reference its frequency with a heterodyne beat note to the output of the isolated DFB laser. We then scan the ECL across the resonance in the backward direction and monitor the transmission. To distinguish the probe transmission from the large feedback from the DFB, we modulate the probe and use a lock-in amplifier after photodetection (Supplementary Section 10). We then measure the frequency offset between the clockwise (resonant with the DFB) and anticlockwise (resonant with the ECL) modes using our heterodyne frequency reference. Figure 4d shows the trace from the lock-in amplifier, exhibiting a frequency splitting of 172 MHz. As the ring resonances have a half-width at half-maximum linewidth of 34.6 MHz (Supplementary Section 6), this splitting corresponds to an isolation of 14 dB, in agreement with the measurement in Fig. 4a (assuming 33 mW input power). Second, we directly measure the transmission of pulses backwards through the ULS device with the DFB laser on and off (Fig. 4e). To do this, we ensure the ECL probe is at the same frequency as the DFB pump using their heterodyne beat note. As the probe and pump are at the same frequency, we extract the transmission from the direct current (DFB feedback) and alternating current (ECL pulse and DFB feedback heterodyne) components. We again find an isolation ratio that is in agreement with Fig. 4a,d.

In this system, the combination of thermal locking and self-injection locking allows for laser stability without external feedback loops. In Fig. 4f we demonstrate the robustness of this type of laser system: when the laser is locked, it can be fully turned on and off over the timescale of at least tens of seconds. Without the self-injection locking feedback, the ring would need to be thermally tuned each time upon start-up to align its transmission spectrum with the laser. Finally, we ensure that this topology is still capable of taking advantage of the rich dynamics that traditional self-injection-locked lasers exhibit[20,32,38,44]. The control of feedback phase is a critical feature to enable or to avoid the comb formation when self-injection locked[32] (Supplementary Section 11). By tuning the coupling gap and thus feedback phase with a piezoelectric positioner, we can observe both continuous-wave and frequency comb operation, and even second harmonic generation (Supplementary Sections 11 and 12)[40].

Conclusion

In this work, we have demonstrated a complete on-chip laser system with narrow linewidth and built-in optical isolation. To realize this, we combined self-injection locking and isolation in a single CMOS-compatible silicon nitride ULS. Although past self-injection schemes function well at low power, we show that they fail to function at higher powers. We propose a device topology that provides strong feedback independent of input power while simultaneously providing isolation. Our fabricated devices passively isolate an integrated DFB laser by 14 dB while simultaneously reducing its frequency noise by 25–35 dB, and operate with turnkey reliability. By increasing the device quality factor through commercial scale fabrication[42], the isolation and noise reduction can be even further enhanced, and the power threshold for operation can be reduced (Fig. 2 and Supplementary Section 13). Although we have demonstrated a ULS that stabilizes a laser by injection locking, a ULS could instead be used as one of the mirrors inside of a laser cavity itself. This would lead to a lower insertion loss, enabling even higher isolation and narrower linewidths. As many hybrid and heterogeneously integrated photonics already include low-loss silicon nitride or similar materials, these devices can be readily integrated into state-of-the-art systems for sensing, metrology and quantum technologies.

Online content

Any methods, additional references, Nature Portfolio reporting summaries, source data, extended data, supplementary information, acknowledgements, peer review information; details of author contributions and competing interests; and statements of data and code availability are available at https://doi.org/10.1038/s41566-024-01539-3.

References

1. Kikuchi, K. Fundamentals of coherent optical fiber communications. *J. Lightwave Technol.* **34**, 157–179 (2015).
2. McGrew, W. et al. Atomic clock performance enabling geodesy below the centimetre level. *Nature* **564**, 87–90 (2018).
3. Daley, A. J. et al. Practical quantum advantage in quantum simulation. *Nature* **607**, 667–676 (2022).
4. Yang, K. Y. et al. Multi-dimensional data transmission using inverse-designed silicon photonics and microcombs. *Nat. Commun.* **13**, 7862 (2022).
5. Rizzo, A. et al. Massively scalable Kerr comb-driven silicon photonic link. *Nat. Photon.* **17**, 781–790 (2023).
6. Feldmann, J. et al. Parallel convolutional processing using an integrated photonic tensor core. *Nature* **589**, 52–58 (2021).
7. Ashtiani, F., Geers, A. J. & Aflatouni, F. An on-chip photonic deep neural network for image classification. *Nature* **606**, 501–506 (2022).
8. Pai, S. et al. Experimentally realized in situ backpropagation for deep learning in photonic neural networks. *Science* **380**, 398–404 (2023).
9. Trocha, P. et al. Ultrafast optical ranging using microresonator soliton frequency combs. *Science* **359**, 887–891 (2018).
10. Rogers, C. et al. A universal 3D imaging sensor on a silicon photonics platform. *Nature* **590**, 256–261 (2021).
11. Li, B., Lin, Q. & Li, M. Frequency–angular resolving lidar using chip-scale acousto-optic beam steering. *Nature* **620**, 316–322 (2023).
12. Wang, J., Sciarrino, F., Laing, A. & Thompson, M. G. Integrated photonic quantum technologies. *Nat. Photon.* **14**, 273–284 (2020).

13. Madsen, L. S. et al. Quantum computational advantage with a programmable photonic processor. *Nature* **606**, 75–81 (2022).
14. Zheng, Y. et al. Multichip multidimensional quantum networks with entanglement retrievability. *Science* **381**, 221–226 (2023).
15. Zhou, Z. et al. Prospects and applications of on-chip lasers. *eLight* **3**, 1 (2023).
16. Liu, A. Y., Komljenovic, T., Davenport, M. L., Gossard, A. C. & Bowers, J. E. Reflection sensitivity of 1.3 μm quantum dot lasers epitaxially grown on silicon. *Opt. Express* **25**, 9535 (2017).
17. Dong, B. et al. Dynamic performance and reflection sensitivity of quantum dot distributed feedback lasers with large optical mismatch. *Photon. Res.* **9**, 1550 (2021).
18. Matsui, Y. et al. Low-chirp isolator-free 65-GHz-bandwidth directly modulated lasers. *Nat. Photon.* **15**, 59–63 (2021).
19. Tkach, R. & Chraplyvy, A. Regimes of feedback effects in 1.5-μm distributed feedback lasers. *J. Lightwave Technol.* **4**, 1655–1661 (1986).
20. Jin, W. et al. Hertz-linewidth semiconductor lasers using CMOS-ready ultra-high-Q microresonators. *Nat. Photon.* **15**, 346–353 (2021).
21. Guo, J. et al. Chip-based laser with 1-hertz integrated linewidth. *Sci. Adv.* **8**, eabp9006 (2022).
22. Herrmann, J. F. et al. Mirror symmetric on-chip frequency circulation of light. *Nat. Photon.* **16**, 603–608 (2022).
23. Yu, M. et al. Integrated electro-optic isolator on thin-film lithium niobate. *Nat. Photon.* **17**, 666–671 (2023).
24. Tian, H. et al. Magnetic-free silicon nitride integrated optical isolator. *Nat. Photon.* **15**, 828–836 (2021).
25. Del Bino, L., Silver, J. M., Stebbings, S. L. & Del'Haye, P. Symmetry breaking of counter-propagating light in a nonlinear resonator. *Sci. Rep.* **7**, 43142 (2017).
26. Del Bino, L. et al. Microresonator isolators and circulators based on the intrinsic nonreciprocity of the Kerr effect. *Optica* **5**, 279–282 (2018).
27. White, A. D. et al. Integrated passive nonlinear optical isolators. *Nat. Photon.* **17**, 143–149 (2023).
28. Schawlow, A. L. & Townes, C. H. Infrared and optical masers. *Phys. Rev.* **112**, 1940 (1958).
29. Li, B. et al. Reaching fiber-laser coherence in integrated photonics. *Opt. Lett.* **46**, 5201–5204 (2021).
30. Xiang, C. et al. High-performance lasers for fully integrated silicon nitride photonics. *Nat. Commun.* **12**, 6650 (2021).
31. Voloshin, A. S. et al. Dynamics of soliton self-injection locking in optical microresonators. *Nat. Commun.* **12**, 235 (2021).
32. Lihachev, G. et al. Platicon microcomb generation using laser self-injection locking. *Nat. Commun.* **13**, 1771 (2022).
33. Xiang, C. et al. 3D integration enables ultralow-noise isolator-free lasers in silicon photonics. *Nature* **620**, 78–85 (2023).
34. Shim, E. et al. Tunable single-mode chip-scale mid-infrared laser. *Commun. Phys.* **4**, 268 (2021).
35. Corato-Zanarella, M. et al. Widely tunable and narrow-linewidth chip-scale lasers from near-ultraviolet to near-infrared wavelengths. *Nat. Photon.* **17**, 157 (2023).
36. Lihachev, G. et al. Low-noise frequency-agile photonic integrated lasers for coherent ranging. *Nat. Commun.* **13**, 3522 (2022).
37. Snigirev, V. et al. Ultrafast tunable lasers using lithium niobate integrated photonics. *Nature* **615**, 411–417 (2023).
38. Li, B. et al. High-coherence hybrid-integrated 780 nm source by self-injection-locked second-harmonic generation in a high-Q silicon-nitride resonator. *Optica* **10**, 1241 (2023).
39. Ling, J. et al. Self-injection locked frequency conversion laser. *Laser Photon. Rev.* **17**, 2200663 (2023).
40. Clementi, M. et al. A chip-scale second-harmonic source via self-injection-locked all-optical poling. *Light Sci. Appl.* **12**, 296 (2023).
41. Kondratiev, N. et al. Self-injection locking of a laser diode to a high-Q WGM microresonator. *Opt. Express* **25**, 28167 (2017).
42. Liu, J. et al. High-yield, wafer-scale fabrication of ultralow-loss, dispersion-engineered silicon nitride photonic circuits. *Nat. Commun.* **12**, 2236 (2021).
43. Yuan, Z. et al. Correlated self-heterodyne method for ultra-low-noise laser linewidth measurements. *Opt. Express* **30**, 25147–25161 (2022).
44. Shen, B. et al. Integrated turnkey soliton microcombs. *Nature* **582**, 365 (2020).

Methods

Device fabrication

Silicon nitride thin films (310 nm) were deposited on silicon dioxide/silicon wafers through low-pressure chemical vapour deposition. The devices were then patterned using a ZEP520A resist and e-beam lithography (JEOL JBX-6300FS). After development, the patterns were transferred to the silicon nitride using inductively coupled plasma etching with CHF_3/CF_4 chemistry. The devices were then cleaned with Piranha solution, annealed at 1,100 °C in a nitrogen environment, and oxide clad using spun hydrogen silsesquioxane and thermal oxide. The devices were annealed a final time under the same conditions and laser stealth diced to create clean facets.

Frequency splitting measurement

We implement the set-up shown in Supplementary Fig. 11 to measure the frequency splitting of the clockwise and anticlockwise ring modes when pumped with the DFB laser. We couple the DFB laser (PhotonX) directly to the chip and use a grating coupler and fibre-coupled circulator to extract the laser power from the output. We then beat this output with a tap-off from a tunable ECL (Toptica) on a photodiode and use the beat note to tune the ECL to frequency degeneracy with the DFB. We can then scan the tunable laser frequency over time and track the frequency-dependent transmission. To recover the frequency-dependent transmission of the ECL over the large amount of backward-going DFB power, we modulate the ECL with an electro-optic modulator and use a lock-in amplifier to read out the transmission. Note that, for clarity, the transmission at low offset frequency is not shown in Fig. 4d because it contains heterodyne noise that does not represent transmission.

Pulsed isolation measurement

We implement the set-up shown in Supplementary Fig. 12 to measure the backward transmission of a pulsed backward signal. Here we also use the heterodyne beat note between the DFB laser and the tunable ECL to tune the ECL to the same frequency as the DFB. We then modulate the ECL with 10 MHz pulses using an electro-optic modulator and monitor the backward transmission without tuning the ECL. As the backwards transmission is at the same frequency as the DFB pump, the photodiode generates a beat note at the modulation frequencies. We measure this beat note by amplifying the photodiode output with a transimpedance amplifier and high pass filtering the resulting signal to remove low-frequency and flicker noise. We then record both the beat note and the much larger direct current component (with the high pass filter removed). Using the beat note and direct current component, we can back-calculate the original signal. To compare the transmission with the un-pumped (laser off) transmission, we make the same measurement without the DFB laser, ensuring that the ECL is tuned onto resonance with the ring resonator. Note that the noise floor of the laser off measurement in Fig. 4e is clipped off to not obscure laser on data.

Thermorefractive noise simulations

To verify whether the frequency noise of our device reached the thermal limit, we closely followed refs. 45,46 to simulate TRN and the corresponding resonance frequency fluctuations in the ring resonator. Thermal noise was found using the fluctuation–dissipation theorem and finite-element method (COMSOL Multiphysics). Specifically, we added a harmonic perturbative heat source in the system with the same spatial distribution as the fundamental waveguide eigenmode, solved the heat transfer equation in the frequency domain, calculated the dissipated heat energy during one cycle, and used the fluctuation–dissipation theorem to convert dissipated heat energy to frequency fluctuations. In the simulations, we assumed a 4,000 × 310 nm Si_3N_4 waveguide (R = 100 µm) surrounded by SiO_2 cladding (2.5 µm on top, 5 µm on bottom) with air above and silicon substrate below. The material properties used in the simulation and a more detailed analysis of TRN (temperature dependency, effects of device geometry) are described in Supplementary Section 1.

Data availability

All data are available from the corresponding authors on reasonable request.

References

45. Kondratiev, N. M. & Gorodetsky, M. L. Thermorefractive noise in whispering gallery mode microresonators: analytical results and numerical simulation. *Phys. Lett. A* **382**, 2265–2268 (2018).
46. Huang, G. et al. Thermorefractive noise in silicon-nitride microresonators. *Phys. Rev. A* **99**, 061801 (2019).

Acknowledgements

A.W. acknowledges the Herb and Jane Dwight Stanford Graduate Fellowship (SGF) and the NTT Research Fellowship. G.H.A. acknowledges support from STMicroelectronics Stanford Graduate Fellowship (SGF) and Kwanjeong Educational Foundation. Authors from Stanford University and UCSB acknowledge funding support from DARPA under the LUMOS programme. Authors from University of Washington acknowledge funding support from NSF under NSF-QII-TAQS-1936100. Part of this work was performed at the Stanford Nano Shared Facilities (SNSF)/Stanford Nanofabrication Facility (SNF), supported by the National Science Foundation under award ECCS-2026822.

Author contributions

A.D.W., G.H.A., and K.V.G. conceived of the project. A.D.W., G.H.A., R.L., and K.V.G. performed the experiments. G.H.A. developed the silicon-nitride fabrication process and fabricated the devices with assistance from A.S. and A.M. J.G., T.J.M., L.C. and J.E.B. provided the semiconductor laser chip and experimental guidance. J.V. supervised the project. All authors contributed to data analysis and writing of the paper.

Competing interests

A.D.W., G.H.A., K.V.G. and J.V. have filed a patent application for the ULS laser architecture (PCT/US2023/032287). The other authors declare no competing interests.

Additional information

Supplementary information The online version contains supplementary material available at https://doi.org/10.1038/s41566-024-01539-3.

Correspondence and requests for materials should be addressed to Alexander D. White or Geun Ho Ahn.

Peer review information *Nature Photonics* thanks Pascal Del'Haye and the other, anonymous, reviewer(s) for their contribution to the peer review of this work.